Biomaterials 112 (2017) 336–345

Contents lists available at ScienceDirect

Biomaterials

journal homepage: www.elsevier.com/locate/biomaterials

# MRI/optical dual-modality imaging of vulnerable atherosclerotic plaque with an osteopontin-targeted probe based on $Fe_3O_4$ nanoparticles

Hongyu Qiao [a, b, 1], Yabin Wang [a, 1], Ruohan Zhang [c, 1], Quansheng Gao [f], Xiao Liang [d], Lei Gao [a], Zhenhua Jiang [b], Ruirui Qiao [e], Dong Han [b], Yan Zhang [a], Ya Qiu [a], Jie Tian [d], Mingyuan Gao [e, **], Feng Cao [a, b, *]

[a] Department of Cardiology, Chinese PLA General Hospital, Beijing, 100853, China
[b] Department of Cardiology, Xijing Hospital, Fourth Military Medical University, Xi'an, 710032, China
[c] Department of Hepato-Biliary and Pancreto-Splenic Surgery, Xijing Hospital, Fourth Military Medical University, Xi'an, 710032, China
[d] Institute of Automation, Chinese Academy of Sciences, Beijing, 100190, China
[e] Institute of Chemistry, Chinese Academy of Sciences, Bei Yi Jie 2, Zhong Guan Cun, Beijing, 100190, China
[f] Laboratory of the Animal Center, Academy of Military Medical Science, Beijing, 100850, China

ARTICLE INFO

*Article history:*
Received 21 April 2016
Received in revised form
22 August 2016
Accepted 10 October 2016
Available online 11 October 2016

*Keywords:*
Dual-modality molecular imaging
Atherosclerotic plaques
Macrophages
Nanoparticles

ABSTRACT

Rupture of vulnerable atherosclerotic plaque is the major pathological cause of luminal thrombosis in acute coronary syndromes. Since foamy macrophages have been identified as a prominent component in vulnerable atherosclerotic lesions and osteopontin (OPN) is reported to be highly expressed in foamy macrophages, OPN could be a potential target for vulnerable atherosclerotic plaque imaging. The current study designed an OPN-specific MRI/optical dual-modality probe to detect vulnerable plaques. Fluorescence imaging revealed that 24 h after injection of the Cy5.5-OPN-DMSA-MNPs (COD-MNPs), the atherosclerotic plaques in carotid artery exhibited significant higher signals in high fat diet (HFD) fed mice in comparison to the group injected with Cy5.5-IgG-DMSA-MNPs (CID-MNPs) or normal diet fed group injected with COD-MNPs ($1.87 \pm 0.19 \times 10^{10}$ vs. $0.74 \pm 0.04 \times 10^{10}$, $0.73 \pm 0.03 \times 10^{10}$ p/sec/cm$^2$/sr, $P < 0.05$). Meanwhile, MRI displayed stronger $T_2$ contrast enhancement 24 h post-injection at the area of atherosclerotic plaques in the carotid of HFD fed group injected with COD-MNPs than group injected with CID-MNPs or normal diet fed group injected with COD-MNPs (post/pre signal ratio: $0.64 \pm 0.04$ *vs.* $0.95 \pm 0.02$, $0.98 \pm 0.01$, $P < 0.05$). As a dual-modality molecular probe, the resulting COD-MNPs conjugates exhibit promising potentials for noninvasive detection of vulnerable atherosclerotic plaque *in vivo*.

© 2016 Elsevier Ltd. All rights reserved.

## 1. Introduction

According to World Health Organization (WHO) 2012 annual report, there were 17.5 million deaths due to cardiovascular diseases, which amounted to 31% of total deaths worldwide [1]. The exacerbation of coronary heart disease (CHD) and stroke lead to approximately 1.2 million deaths yearly [2]. Atherosclerosis is the major pathological cause of cardiovascular disease, and pathology studies have confirmed the common association of acute myocardial infarction with the rupture or erosion of a coronary atherosclerotic plaque [3,4]. Clinical investigations have shown that greater than half of patients afflicted with coronary atherosclerosis suffering from sudden death or myocardial infarction as the first clinical manifestation of disease [5]. Therefore, effectively evaluating and predicting the rupture of atherosclerotic plaques are in great need, but remain practically challenging.

Current clinical diagnosis imaging techniques for atherosclerosis include X-ray contrast angiography, intravascular ultrasound (IVUS), carotid ultrasound, and optical coherence tomography (OCT) [6,7], *etc*. Among them, the X-ray contrast angiography has been adopted as gold-standard method for detecting the severity of

* Corresponding author.
** Corresponding author.
*E-mail addresses:* gaomy@iccas.ac.cn (M. Gao), wind8828@gmail.com (F. Cao).
[1] These authors contributed equally to this work.

http://dx.doi.org/10.1016/j.biomaterials.2016.10.011
0142-9612/© 2016 Elsevier Ltd. All rights reserved.

coronary luminal obstruction; IVUS based on the spectral analysis of backscattered radio frequency signal is able to provide the information of plaque components including necrotic core, dense calcium, fibrous, and fibrofatty plaque; OCT offers high resolution by employing near-infrared light to obtain detailed morphological information. However, the use of plaque contrast features may cause confusion in accurate determination of the plaques' compositions.

To better understand the molecular aspects of atherosclerosis rather than the luminal compromise, molecular imaging based on noninvasive imaging techniques has become a new trend for the assessment of plaque vulnerability [8,9]. And, the development of suitable molecular probes is the most important issue for imaging of vulnerable plaque *in vivo*.

Vulnerable atherosclerotic plaques are characterized with focal inflammation, abundant apoptotic cells, large necrotic cores, and thin fibrous caps [10,11]. Macrophages, especially foamy macrophages are the key inflammatory cells that are involved in focal inflammation and can secrete metalloproteinase and collagenase to weaken the fibrous cap and render plaques liable to rupture [12]. Therefore, foamy macrophages are crucial in vulnerability of plaques and can potentially be target cells for detecting vulnerable plaques.

Osteopontin (OPN) is a secreted protein serving as a chemotactic cytokine with pleiotropic functions promoting the adhesion, migration and activation of foamy macrophages [13,14]. OPN has been identified to be overexpressed by foamy macrophages in human atherosclerotic lesions [15], which was demonstrated by western blot and immunohistochemical assays at both protein and tissue levels [16,17]. Therefore, it is a suitable target for evaluating the vulnerability of plaques through foamy macrophages imaging.

Our previous investigations on detection of atherosclerotic plaques demonstrated that Profilin-1 can be used to effectively target vascular smooth muscle cells [18]. Besides the imaging of smooth muscle cells, we further investigate the molecular imaging technique for the foamy macrophages in the vulnerable plaques. Herein, we report a dual-modality probe based on $Fe_3O_4$ nanoparticles and Cy5.5-labeled OPN antibody to target foamy macrophages. Careful *in vitro* experiments were performed to characterize the targeting ability of the designed probe for foamy macrophages. Both *in vivo* MRI and optical imaging were carried out for visualizing the vulnerable plaques in an atherosclerosis model with the aid of the above dual-modality probe.

## 2. Materials and methods

### 2.1. Animals and procedures

All animal studies were performed according to a protocol approved by the Fourth Military Medical University (FMMU) Animal Care and Use Committee. 20 female 15 g 6-week-old $ApoE^{-/-}$ mice (C57BL/6J genetic background) (Vital River, Beijing) were fed with high fat diet (HFD) (containing 15% fat and 1.25% cholesterol) continually for 20 weeks to establish the atherosclerosis model. Mice of control group were fed with normal diet. All the procedures were performed in accordance with the Fourth Military Medical University Guide for the Care and Use of Laboratory Animals formulated by the National Society for Medical Research.

### 2.2. Reagents and antibodies

RPMI 1640 culture medium and fetal bovine serum (FBS) were obtained from Gibco (Grand Island, USA). Rabbit anti-mouse CD68, OPN antibody were purchased from Abcam (Cambridge, UK) (1:1000 for Western blot, 1:200 for immunofluorescence staining). 3-(4,5-dimethyl-2-thiazolyl)-2,5-diphenyl-2-H-tetrazolium bromide (MTT) (Sigma-Aldrich, St Louis, MO, USA), in Situ Cell Death Detection Kit, POD (Roche, Shanghai), Raw 264.7 macrophage (Bo Gu Biology Technology, Shanghai), Cy5.5-NHS (GE Healthcare, Piscataway, USA), iron acetylacetonate ($Fe(acac)_3$) (Sigma-Aldrich, St. Louis, USA), meso-2,3-dimercaptosuccinic acid (DMSA), 1-ethyl-3-(3-dimethyaminopropyl) carbodiimide (EDC), and *sulfo*-N-hydroxysuccinimide (*sulfo*-NHS) (Sigma-Aldrich, St. Louis, USA) were used as received.

### 2.3. Preparation of COD-MNPs

The synthesis of $Fe_3O_4$ magnetic nanoparticles (MNPs) was carried out as reported before [19]. $Fe(acac)_3$ was used as an iron precursor and oleic and oleylamine were used as surfactant. Then hydrophilic modification of MNPs' surface was accomplished by ligand exchanging reaction with DMSA. Cy5.5-labeled OPN antibody was conjugated with DMSA-coated MNPs (DMSA-MNPs) based on amidation reaction mediated by EDC/*sulfo*-NHS. Briefly, 2 mg EDC (10 mg/mL) and 3 mg *sulfo*-NHS (10 mg/mL) were added in 10 mL aqueous solution of DMSA-MNPs (1 mg/mL) at room temperature. 45 min later, adequate 0.4 mL aqueous solution of OPN antibody (25 mg/mL) pre-labeled with Cy5.5 through reaction with Cy5.5-NHS were introduced dropwise and the reaction mixture was persistently stirred for 12 h at 4 °C. The redundant Cy5.5 labeled OPN antibody was removed *via* using a strong magnet to absorb the conjugates and abandoning the supernatant. Washed the conjugates with deionized water several times until the supernatant didn't show any fluorescence signal. The resulting Cy5.5-OPN-DMSA-MNPs conjugates denoted as COD-MNPs were stored at 4 °C in the dark for future use, and meanwhile a similarly structured control probe, i.e., Cy5.5-IgG-DMSA-MNPs (CID-MNPs) was prepared and stored in the same way.

### 2.4. Characterizations of probes

For the assessment of nanoparticles' morphology and size, we first diluted the nanoparticles with deionized water to prepare the sample and put a drop on the copper net of electron microscope. After the sample on the copper net was dry, TEM (transmission electron microscopy) (TEM, JEM-2100, JEOL, Tokyo, Japan) with the grid of 300-mesh-copper net was used to obtain images operating at an accelerating voltage of 100 kV. More than 300 particles were measured with the aid of Image J software for calculating the average size of the $Fe_3O_4$ nanoparticles. DLS (dynamic light scattering) (Zetasizer Nano ZS90, Malvern Instruments JEM-100CXII, Worcestershire, UK) equipped with a solid-state He–Ne laser ($\lambda = 633$ nm) was used to characterize samples' hydrodynamic size and zeta potential. The magnetic properties of powder samples were analyzed in a vibrating sample magnetometer (VSM JDM-13, China).

### 2.5. Cell culture and cytotoxicity studies

Mouse macrophage line Raw 264.7 were cultured using RPMI 1640 supplemented with 15% FBS and were maintained in a humidified environment containing 5% $CO_2$ and air at 37 °C. When cells reached 90%, sterile PBS was added and cells were moved by gently rinsing. MTT assay was used to detect cells' survival rate. Briefly, cells ($1 \times 10^4$/well) were seeded in 96-well plate. The following day, probes in different concentrations (0, 5, 10, 15, 20, 25, 30, 50 μg/mL) were incubated with the cells. After 24 h, 20 μL of MTT in PBS (5 mg/mL) was introduced per well and the cells were incubated at 37 °C for 4 h. After the incubation medium was removed, 150 μL of DMSO was added into each well followed by

gentle rocking for 10 min to dissolve the dark blue MTT crystals. Optical density (OD) of each well was detected with an Infinite® F500 micro-plate reader (TECAN, Switzerland) at 490 nm and cell viability of every group was expressed as proportion of the control.

For cells' apoptosis assessment, cells pre-incubated with probes (0, 10, 30, 50 μg/mL) for 24 h were collected for terminal deoxynucleotidyl transferase-mediated dUTP nick end labeling (TUNEL) apoptosis assay using a in Situ Cell Death Detection Kit according to the manufacturer's instructions. DAPI staining was performed for total nuclei quantification. The TUNEL-positive cells were imaged by a confocal fluorescent microscope (Olympus FV 10i, Japan).

For further quantitative analysis of cell apoptosis, $5 \times 10^5$ cells treated with probes of different concentrations, i.e., 0, 10, 30, 50 μg/mL, were harvested and washed with PBS, and then stained with propidium iodide and Annexin V-FITC (BD Pharmingen™) for flowcytometry (BD FACSAria, USA) measurements.

### 2.6. Prussian blue staining and fluorescence detection in vitro

The macrophage-derived foamy macrophages stimulated by Ox-LDL (50 μg/mL) for 24 h were used to examine the uptake of probes in two ways: Prussian blue staining of Fe and fluorescence detection of Cy5.5. For Prussian staining, cells with or without Ox-LDL stimulating were incubated with 30 μg/mL COD-MNPs and CID-MNPs respectively for 24 h. For the blocking group, OPN antibody was added 30 min earlier than the probes, then cells were washed with PBS and fixed in 4% paraformaldehyde for 20 min. After that, a mixture of 5 wt-% potassium ferrocyanide and 10 vol-% HCl with ratio of 1:1 was added. After approximately 15 min of incubation, Milli-Q water was used to wash cells three times, which was followed by microscopy studies with an Olympus BX51 inverted microscope (Olympus, Japan).

For fluorescence detection, cells were seeded in 35 mm coverglass-bottom dishes. After fixation, cells were washed with PBS and then 4′, 6-diamidino-2-phenylindole (DAPI) was added for nuclei staining. Images were acquired with confocal fluorescent microscope (Olympus FV 10i, Japan).

### 2.7. Serum lipid analysis and oil red staining

The serum was separated after coagulation of the blood sample. Then, serum levels of triglycerides (TG) and total cholesterol (TC) were analyzed *via* enzyme linked immunosorbent assay (ELISA). For oil red staining, vascular tissues from carotid artery to abdominal aorta of the mice were harvested, then the tissues were embedded in 4% phosphate buffered formaldehyde for 20 min and stained with oil red dye. Pictures were taken after the unreacted staining reagents was washed away with 60% isopropanol.

### 2.8. Immunohistochemistry staining

H&E, Masson's trichrome and immunofluorescence staining stain were performed to analyze the histology and the expression of OPN in atherosclerotic plaques. Artery with plaques were embedded in OCT and snap-frozen. Transverse and radial cryosections (10 μm thick) were collected, fixed in cold acetone, and stained with OPN antibody and DAPI for nuclei. Images were taken by confocal fluorescent microscope (Olympus FV 10i, Japan).

### 2.9. Fluorescence/MRI imaging

Fluorescence imaging was performed by IVIS Kinetic System (Caliper Life Sciences, Hopkinton, USA). For *in vitro* cell imaging, COD-MNPs probes were used in different concentrations, i.e., 0, 5, 15, 30, and 50 μg/mL. Regarding *in vivo* imaging, mice were firstly anaesthetized by isoflurane and then *in vivo* images were taken before and 24 h, 48 h, 72 h after 100 μL COD-MNPs (5 mg Fe/kg) or CID-MNPs were injected through tail vein, respectively. In the meantime, the vessels of some HFD-fed mice were also isolated 48 h post-injection from carotid to abdominal aorta for the following *in vitro* imaging. The imaging parameters were set as follows: binning, 2; F/stop 2; exposure time, 30.0 s; emission filter, Cy5.5. Bioluminescent signals were analyzed using Living Image 4.0 software (Caliper, MA, USA) and quantified as average radiance (p/sec/cm$^2$/sr).

For *in vitro* MRI imaging, 200 μL of aqueous solution of the probes with concentration of 0, 3.25, 7.5, 15, 30 μg/mL were adopted for cell labelling. Regarding *in vivo* MRI imaging, mice were also anaesthetized by isoflurane, and then images were acquired before and 24 h after intravenous injection of 100 μL probe solution through tail vein (Fe concentration was: 1 mg/mL). Images were acquired on a 1T M3™ Compact High-Performance MRI System (Aspect Imaging, Israel) with parameters set as follows: vertical field of view (FOV) 30 mm, horizon field of view (FOV) 30 mm; base resolution, 256 × 256, slice thickness 0.8 mm, time to echo (TE) 62.77 ms, repetition time (TR) 1500 ms. Because the plaque was usually located just above the carotid bifurcation, for each sequence, interested region was chosen to be the plaque in the common carotid artery and plaque the internal carotid artery. Typical images were obtained in accordance to the previous papers [20,21]. And we analyzed the DICOM data exported from the MRI System using VivoQuant 1.23 software (inviCRO, America). The $T_2$-weighted signal change was calculated by using the following formula: $SI_{post}/SI_{pre} \times 100\%$, where $SI_{pre}$ and $SI_{post}$ were the signal intensity of the atherosclerotic plaques in carotid artery before and 24 h after administration of the probe, respectively.

### 2.10. Western blot analysis

Cells preconditioned with/without Ox-LDL for 24 h were harvested. Protein concentrations were determined with a bicinchoninic acid (BCA) assay kit (Pierce, Rockford, IL). The proteins were separated by 10% SDS-PAGE gels and transferred onto nitrocellulose membrane. Membranes were blocked with Tris buffered saline-Tween-20 containing 5% non-fat milk and incubated with OPN primary antibodies overnight at 4 °C. The membranes were incubated with secondary antibodies (Abcam, Cambridge, MA, USA) conjugated with horseradish peroxidase for 1 h. The target protein was detected by enhanced chemiluminescene system (Amersham Bioscience, Fairfield, Connecticut, USA) and quantified by Quantity One Analysis Software (version 4.5, Bio-Rad, USA).

### 2.11. Statistical analysis

Continuous variables that approximated the normal distribution were expressed by mean ± standard deviation (SD). Multiple group comparisons were performed by one-way analysis of variance (ANOVA) followed by the least significant difference (LSD) *t*-test for *post hoc* analysis. Comparisons between the two independent groups were analyzed using the Student's *t*-test. Two-sided tests were used throughout the experiment. $P < 0.05$ was considered statistically significant. GraphPad Prism-5 statistic software (La Jolla, CA) was used for all data analysis.

## 3. Results

### 3.1. Characterization of DMSA-MNPs and COD-MNPs probes

Fig. 1a shows a representative transmission electron microscope (TEM) image of DMSA-MNPs which have an average size of

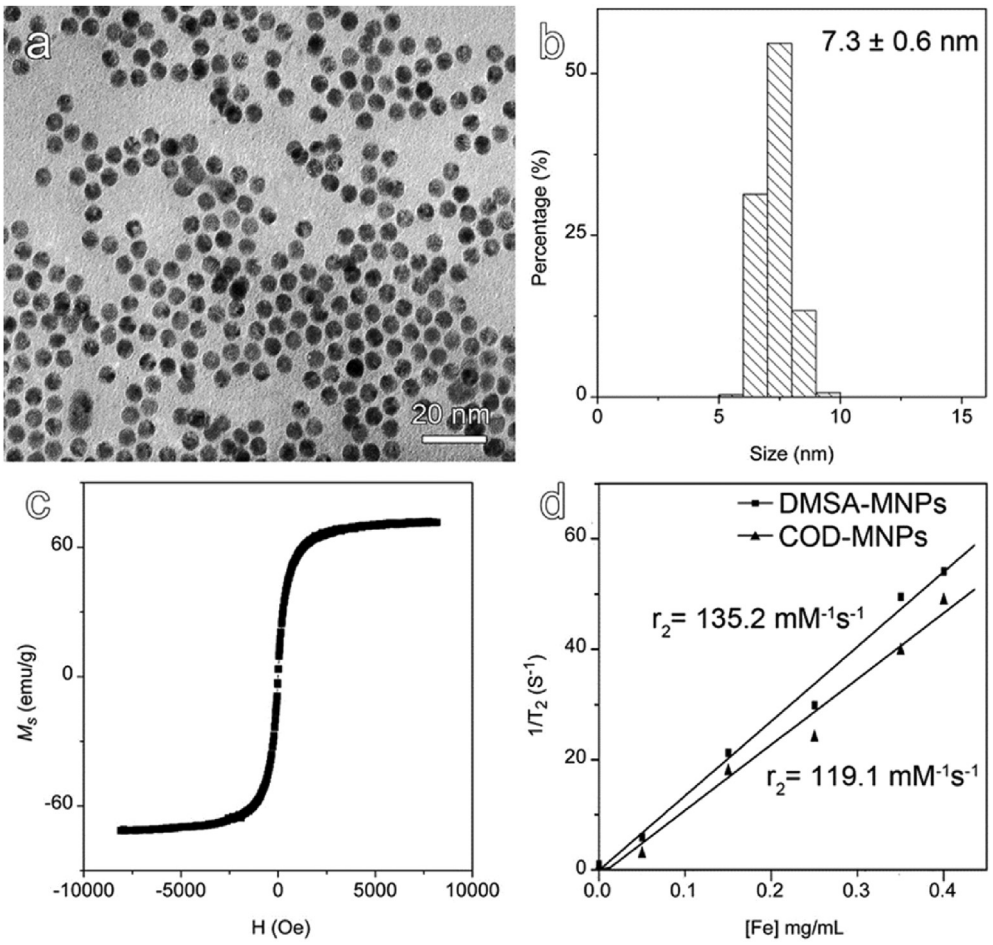


**Fig. 1.** TEM image (a), histogram of particle size (b), saturation magnetization curve (c) of DMSA-MNPs, together with $1/T_2$ plotted against the concentration of Fe (d) for extracting relaxivity ($r_2$) of DMSA-MNPs and COD-MNPs as inserted.

7.3 ± 0.6 nm (Fig. 1b). The room-temperature magnetization curve shown in Fig. 1c demonstrates that the DMSA-MNPs are superparamagnetic with a saturation magnetization up to 62.7 emu/g. The MRI contrast enhancement effect of DMSA-MNPs is shown in Fig. 1d and the transverse relaxivity ($r_2$) is calculated to be 135.2 mM$^{-1}$s$^{-1}$, while the transverse relaxivity ($r_2$) of COD-MNPs is calculated to be 119.1 mM$^{-1}$s$^{-1}$.

The scheme in Fig. 2a describes the conjugation between Cy5.5-labeled OPN antibody and DMSA-MNPs *via* a covalently amidation reaction between the $-NH_2$ group of the antibody and $-COOH$ residue on the surface of DMSA-MNPs. The DLS results in Fig. 2b and c reveals that the hydrodynamic diameter of COD-MNPs was 92.2 ± 3.5 nm and the zeta potential was −52.7 ± 1.1 mV, while DMSA-MNPs was 32.2 ± 4.6 nm and −39.2 ± 2.1 mv respectively, indicating a successful conjugation between the nanoparticles and Cy5.5-labeled anti-OPN antibody. As shown in Fig. 2d, the fluorescence signal intensity exhibited positive correlation with the concentration of Fe. And the *in vitro* experiment of MRI showed that our probe exhibited stronger $T_2$ contrast enhancement effect when the concentration of Fe was higher, which showed darker in the figure. As we know that MRI works based on computer-assisted imaging of relaxation signals of proton spins within the human body excited by radiofrequency waves in a strong magnetic field [22]. And the relaxation of proton spins to their equilibrium states *via* two processes, namely longitudinal relaxation, characterization by a relaxation time $T_1$, and transverse relaxation, characterized by a relaxation time $T_2$. The MRI contrast agents principally work by shortening the $T_1$ or $T_2$ relaxation times of protons located nearby, iron oxide nanoparticles like what we used in the experiment, can effectively reduce the $T_2$ relaxation time and consequently produced negative enhancement effects on $T_2$-weighted images.

### 3.2. Cytotoxicity evaluation of COD-MNPs probe

As displayed in Fig. 3a, in comparison with the control group, the viability of cells incubated with COD-MNPs conjugates don't show significant variation in the concentration range of Fe from 5 to 50 μg/mL, indicating a low cytotoxicity of the resulting probes. To further confirm this feature, TUNEL tests were performed and the results shown in Fig. 3b. Quantitative results showing in the right panel demonstrate that the FITC signal for showing the apoptotic cells dose not vary significantly if comparing the COD-MNPs groups (10, 30 and 50 μg Fe/mL) with the control group, i.e., 6.8 ± 0.3%, 7.1 ± 0.4%, 7.5 ± 0.3% versus 6.6 ± 0.4% from control ($P > 0.05$). Further flow cytometry results given in Fig. 3c reveal that the apoptosis rates of groups with Fe concentration of 10, 30 and 50 μg/mL were 7.0 ± 0.2%, 7.8 ± 0.3% and 7.9 ± 0.2%, respectively, close to that for the control group, i.e., 5.7 ± 0.2% with $P > 0.05$. Both TUNEL and flow cytometry assays demonstrated that the COD-MNPs probes have insignificant influence on the apoptosis of macrophages. They are therefore suitable for the following *in vivo* studies.

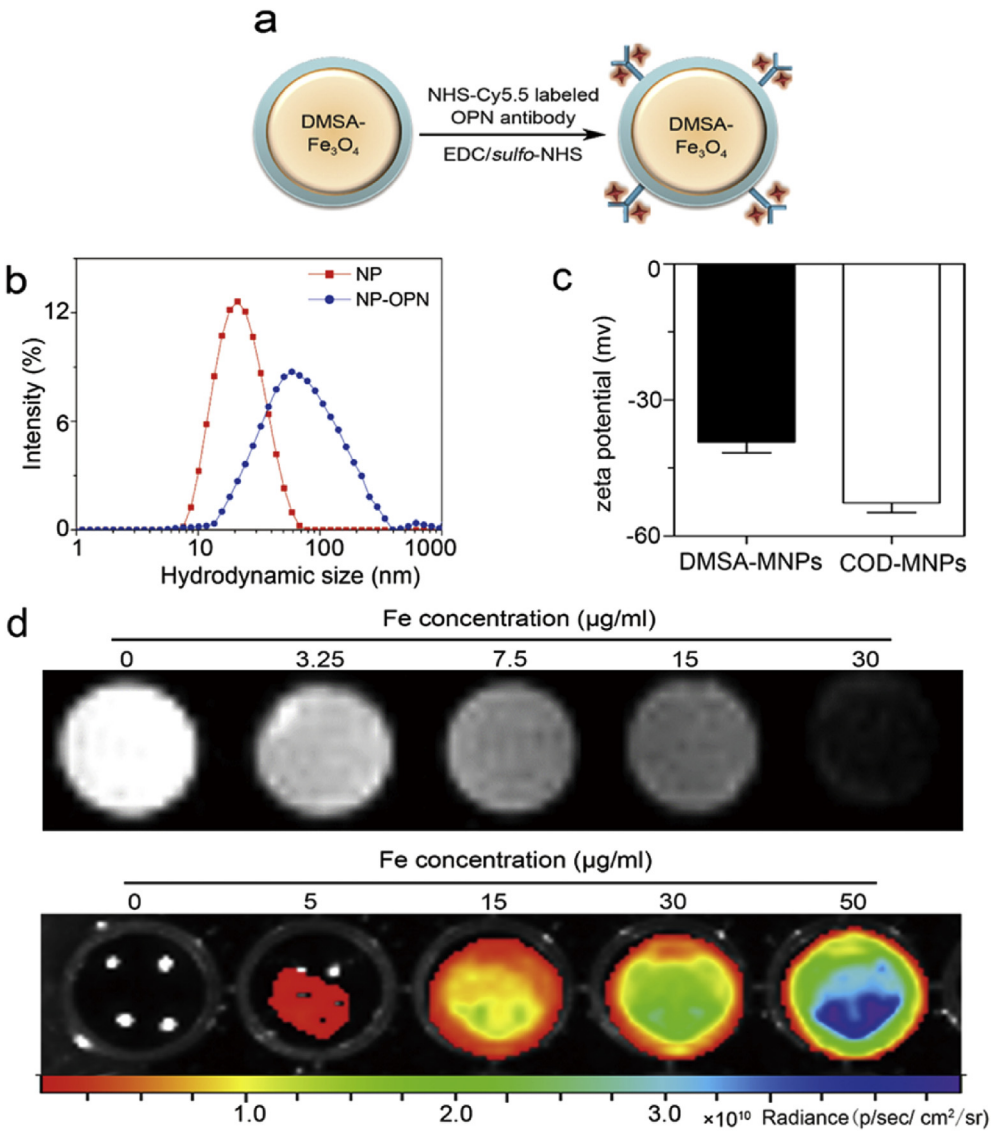


**Fig. 2.** A schematic drawing for COD-MNPs conjugate preparation (a), hydrodynamic profiles of the DMSA-MNPs (NP) and the COD-MNPs conjugates (NP-OPN) (b), zeta potential of DMSA-MNPs, COD-MNPs (c) and MR and fluorescence images of aqueous solutions of COD-MNPs conjugates with different concentrations as indicated (Note: the optical signal was color-coded for better showing the signal variation) (d).

### 3.3. Evaluation of OPN expression in foamy macrophages

To evaluate the OPN expression in macrophages, Raw 264.7 cells were exposed to Ox-LDL to induce the formation of foamy macrophages [23]. As shown in Fig. 4a, the expression of OPN in Ox-LDL stimulated foamy macrophages is much higher than the untreated macrophages. The quantitative results of western blot further confirmed the up-regulated expression of OPN in foamy macrophages (Fig. 4b) with OPN/β-actin value up to 1.31 ± 0.04 contrasting to 0.16 ± 0.02 for control with $P < 0.05$, as shown in Fig. 4b. These results indicate that the OPN is a potential target for vulnerable atherosclerotic plaque detection.

### 3.4. Binding affinity of COD-MNPs

The binding affinity of COD-MNPs was evaluated on foamy macrophages through immunofluorescence and Fe staining assay. As shown in Fig. 4c, the Cy5.5 signal (red) from COD-MNPs is predominantly localized in the cytoplasm of foamy macrophages. In contrast, only very weak signal is presented in the un-stimulated normal macrophages or foamy macrophages co-incubated with CID-MNPs. Moreover, the optical signal is remarkably suppressed when OPN antibody was added for blocking prior to the introduction of COD-MNPs. The Fe staining results given in Fig. 4d show rather consistent tendency, indicating that COD-MNPs probes possess good binding specificity for targeting foamy macrophages.

### 3.5. Verification of animal atherosclerosis models

In order to demonstrate the *in vivo* imaging capability of COD-MNPs, an atherosclerosis model was established according to literature [24]. To monitor the atherosclerosis, lipid profiles of mice's serum were analyzed. As shown in Fig. S1a, HFD group showed much higher levels of blood cholesterol and triglyceride compared with those for the control group, e.g., cholesterol: 19.7 ± 1.4 mmol/L vs.7.6 ± 1.6 mmol/L, $P < 0.05$; TG: 0.50 ± 0.15 mmol/L vs. 0.20 ± 0.05 mmol/L, $P < 0.05$. To further confirm the formation of atherosclerotic plaques in the HFD mice,

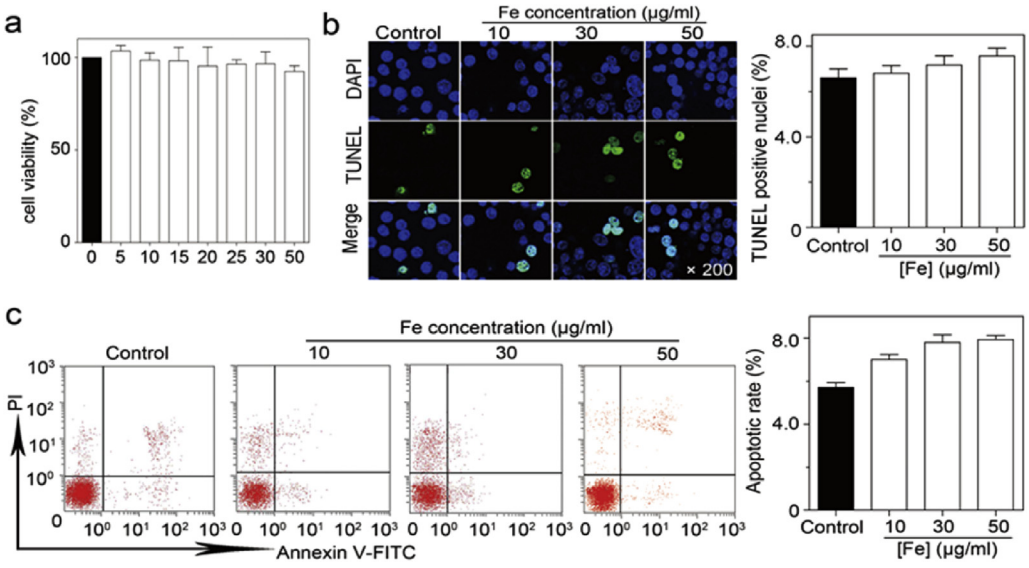


**Fig. 3.** MTT assay (a) TUNEL assay (b) and flow cytometry (c) results for evaluating the cytotoxicity of COD-MNPs conjugates.

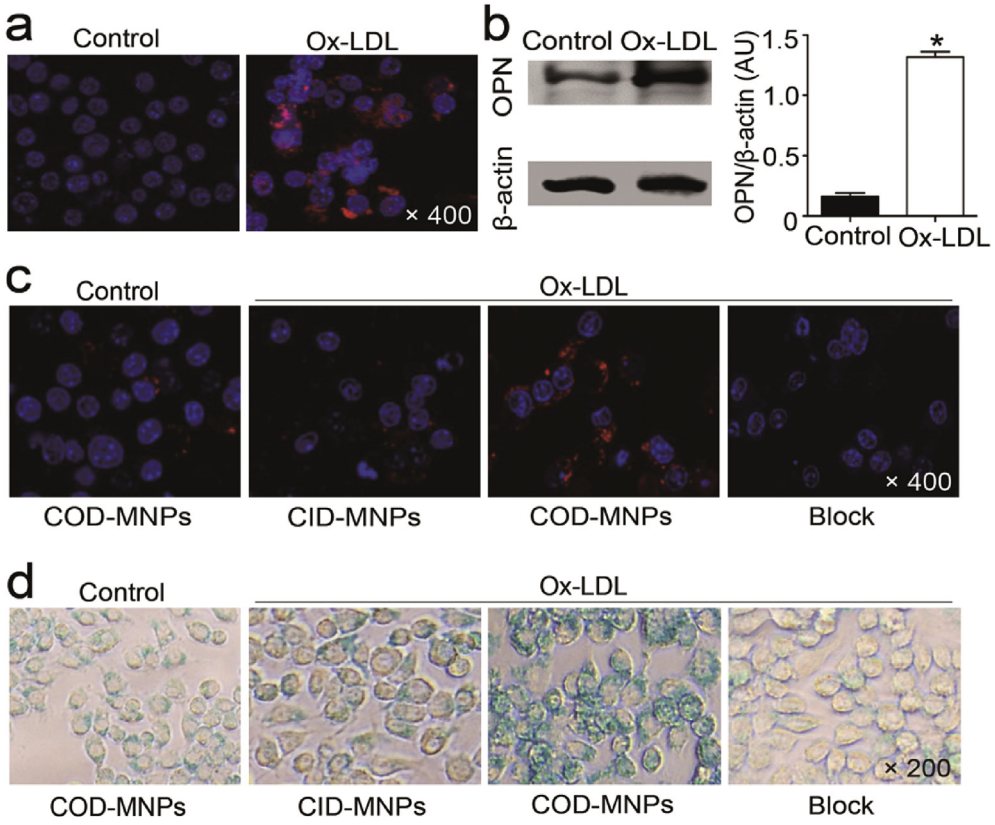


**Fig. 4.** a, confocal microscopy images of macrophages before (left) and after 24 h incubation with Ox-LDL; b, Western blot results for showing the expression of OPN/β-actin in foamy macrophages upon Ox-LDL treatment; c, confocal microscopy images of foamy macrophages and their control after incubation with COD-MNPs CID-MNPs, respectively and the last image (block) was acquired upon addition of OPN antibody prior to the introduction of COD-MNPs; d, Prussian blue staining of macrophages treated the same way.

vascular tissues from carotid to abdominal artery were isolated. The following oil red staining for lipid of plaques revealed that the lesion area is significantly enlarged in HFD fed group in comparison with control group with the ratio of lesion area to whole artery area up to 57% contrasting to 0.5% for the control. H&E and Masson's trichrome staining further confirmed that the lesion exhibit vulnerable atherosclerotic plaques' features such as thin and partly ruptured fibrous cap, cholesterol crystal, and so on (Fig. S1b). Further CD68 staining also led to strong FITC signal (green) around the plaques, as shown in Fig. S2, suggesting abundant accumulation of macrophages showing another major characteristic of vulnerable plaques. Meanwhile, Cy3 signal (red) from OPN staining further

confirm the upregulated expression of OPN in atherosclerotic plaques, which makes it possible for COD-MNPs to target vulnerable plaques. All above studies strongly support the successful establishment of the animal model for vulnerable plaques.

### 3.6. *In vivo* Fluorescence/MRI imaging

Towards targeted detection of vulnerable plaques, *in vivo* fluorescence/MR imaging studies were carried out in the animal atherosclerosis model after intravenous injection of the nanoprobes. Fluorescence images in Fig. 5a reveal that the signal intensity of the plaques in carotid artery is much higher in HFD fed group injected with COD-MNPs than the group injected with CID-MNPs or control group injected with COD-MNPs especially at 48 h post-injection (24 h: $1.87 \pm 0.19 \times 10^{10}$ vs. $0.74 \pm 0.04 \times 10^{10}$, $0.73 \pm 0.03 \times 10^{10}$; 48 h: $7.38 \pm 0.32 \times 10^{10}$ vs. $0.81 \pm 0.05 \times 10^{10}$, $0.81 \pm 0.04 \times 10^{10}$; 72 h: $2.00 \pm 0.30 \times 10^{10}$ vs. $0.73 \pm 0.05 \times 10^{10}$, $0.72 \pm 0.05 \times 10^{10}$ p/sec/cm$^2$/sr, $P < 0.05$). The *in vitro* imaging of vascular tissue isolated from HFD fed group injected with COD-MNPs further supports that the *in vivo* optical signal originated from the carotid artery upon active targeting.

The *in vivo* MRI results, as shown in Fig. 5b, also indicate a clear $T_2$ enhancement effect of COD-MNPs conjugates for plaques in carotid artery with a post/pre signal ratio of $0.64 \pm 0.04$, contrasting to those from the control experiments, i.e., $0.95 \pm 0.02$ for HFD fed group injected with CID-MNPs and $0.98 \pm 0.01$ for the control group of mice injected COD-MNPs.

To verify the active targeting of the specific nanoprobes, Fe staining of plaques was performed and the Prussian Blue staining results shown in Fig. 6 show that the COD-MNPs conjugates are preferentially localized in the atherosclerosis plaques, while H&E and Masson's trichrome staining further reveal the major features of the targeted vulnerable plaques including thin and partly ruptured fibrous cap. In addition, the immunofluorescence results also confirmed the abundant expression of OPN (staining red). All above results prove that COD-MNPs conjugates can specifically target vulnerable plaques *in vivo*.

## 4. Discussion

Molecular imaging based on invasive imaging techniques such as ultrasound, MRI, optical imaging, or PET/CT has been widely explored to detect atherosclerotic plaques. Studies have shown that contrast-enhanced ultrasound (CEUS) can be used to detect intraplaque neovascularization [25,26] and a recent meta-analysis demonstrated that qualitative CEUS has a sensitivity of 80% (95% CI: 0.72–0.87) and a specificity of 83% (95% ci: 0.76–0.89) for detecting intraplaque neovascularization [27]. But a number of drawbacks exist when applying these techniques for detection of atherosclerosis such as motion artifact, limited tissue penetration

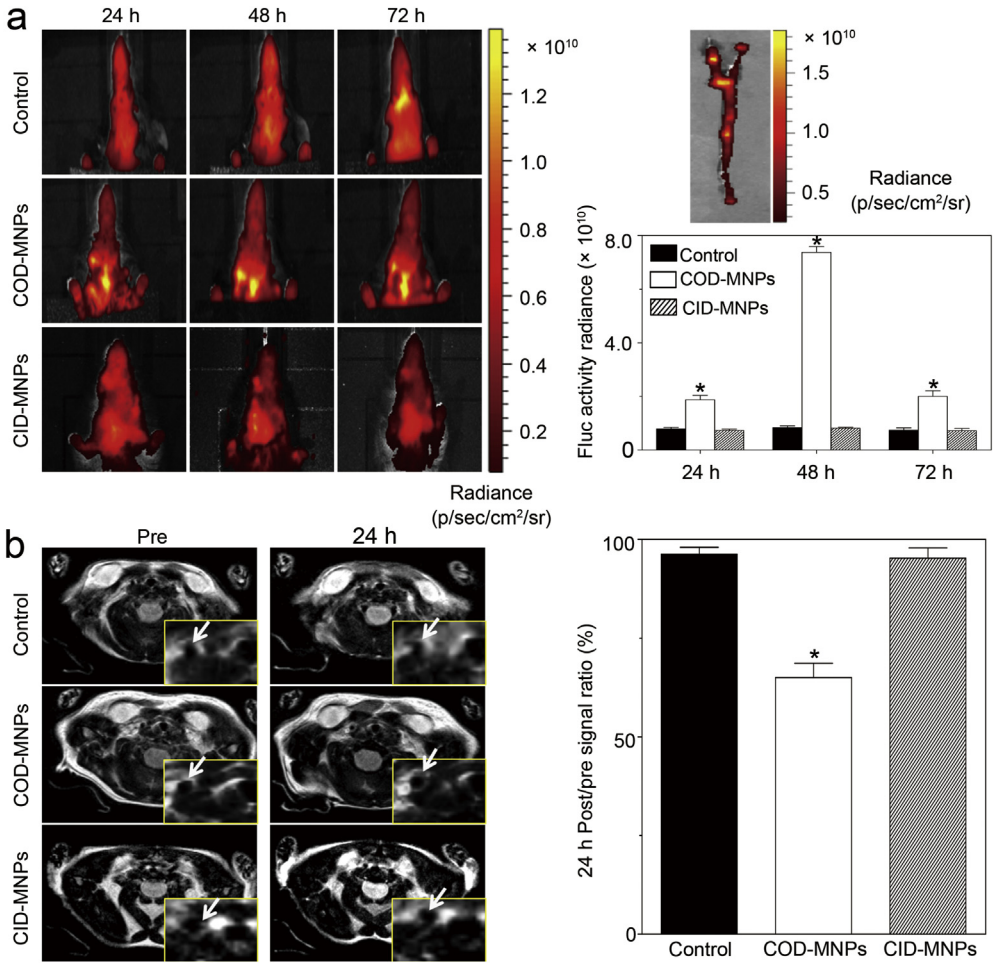


**Fig. 5.** Fluorescence (a) and MR (b) images of HFD fed mice acquired at different time points after intravenous injection of different probes for comparing with those receive no probe injection. The right part of panel (a) shows a fluorescence image of the carotid and aortic arch tissue extracted from a HFD fed mouse 72 h after the administration of COD-MNPs, and the right part of panel (b) shows quantitative *in vivo* $T_2$ signal of region of interest after intravenous injection of COD-MNPs or CID-MNPs, $^*P < 0.05$.

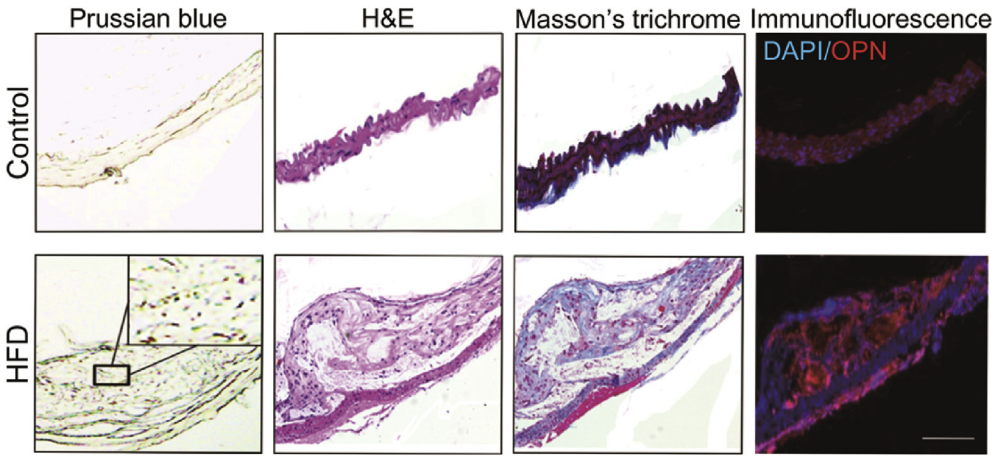


**Fig. 6.** Prussian blue, H&E, Masson's trichrome staining of carotid tissues extracted from mice treated with normal diet (control) and high fat diet (HFD) 72 h after the injection of COD-MNPs conjugates into the latter group. The right-hand group of immunofluorescence images were recorded for showing the expression of OPN in the corresponding tissues.

and spatial resolution. PET imaging has been used to study biologic processes within unstable plaques, for example: $^{18}$F-FDG-inflammation imaging [28] and $^{18}$F-NaF imaging of microcalcification [29], etc. However, because of the radioligands decay, this imaging modality was limited for patients with renal or hepatic impairment. MRI has been demonstrated to be useful in plaque size analysis during the progression or regression of experimental atherosclerosis due to its excellent spatial resolution and the ability to readily co-register anatomic and contrast data [30,31]. Dynamic contrast-enhanced MRI uses the movement kinetics of gadolinium within vascular tissue to derive reasonable surrogates of both plaque inflammation and neovascularization [32]. However, due to the relatively lower contrast sensitivity, MRI still has lots of limitations in detecting plaques. To overcome those limitations, optical imaging has become a complementary for MRI for offering much higher sensitivity in comparison to MRI. The combination of the two imaging tools has provided a more powerful approach for detecting plaques along.

In this study, a dual-modality molecular probe was constructed based on $Fe_3O_4$ nanoparticles for *in vivo* visualization of atherosclerotic plaques through active foamy macrophages targeting. Via antibody-mediated targeting, vulnerable plaques in an ApoE$^{-/-}$ mouse model was successfully detected through both MR and fluorescence imaging approaches. Immunohistochemical analysis further supported the excellent targeting specificity of the probe for non-invasive atherosclerosis diagnosis.

Ideal probe for dual-modality imaging of atherosclerosis should possess good biocompatibility, low cytotoxicity and active targeting ability. Currently, nanoparticles are largely chosen act as probe carrier due to the following advantages: their sizes are comparable to those of biological macromolecules such as proteins; upon proper size and surface engineering, long blood circulation time can be achieved [33]; the large surface to volume ratio provides versatile choice for loading imaging and targeting moieties. Numerous literature demonstrated that iron oxide nanoparticles are non-toxic to cells, organs, or even human bodies [34,35]. In the current study, DMSA was used as surface capping agent to displace the original inorganic surface ligand for rendering $Fe_3O_4$ nanoparticles with water solubility and colloidal stability. MTT, TUNEL assays together with flow cytometry studies suggested that DMSA-coated $Fe_3O_4$ nanoparticles are non-toxic to the macrophage cells below a certain threshold.

Actually, ultrasmall superparamagnetic iron oxide nanoparticles have been reported as MRI contrast agent for atherosclerotic plaques imaging [36]. However, the passive delivery of iron oxide nanoparticles only gives rise to enhancement effect at the plaque site *via* the enhanced vascular permeability resulting from injured endothelium, leaky microvessels, etc [37,38]. Moreover, anatomic assessments of atherosclerosis hardly reflect the corresponding pathophysiology. In difference, the active targeting strategy, depending on the choice of the targets, is more favorable for disclosing the molecular mechanisms associated with the vulnerable risk of given plaques. Endothelial denudation, angiogenesis, local inflammation, the presence of macrophages, thin fibrous cap, lipid or necrotic core are often considered as suitable targets. For example, Nahrendorf et al. utilized $^{18}$F-4V as PET-CT agent to target adhesion molecule-1 which plays an important role in local inflammation [39]; Karen C et al. conjugated MDA2, E06, and IK17 to Gd-loaded microvesicles and used them to target Ox-LDL which is related to macrophages and the lipid pool of the plaques [40]; paramagnetic gadolinium nanoparticles targeted to $\alpha_v\beta_3$-integrins have been shown to image angiogenesis as well as track therapeutic activity in atherosclerosis animal models [41]. Utilizing a different targeting moiety, gadolinium-loaded immunomicelles were targeted to the macrophage scavenge receptor with cell-specific delivery for imaging of plaque-associated macrophages within the atheroma [42]; oxidative stress has been directly monitored using a myeloperoxidase sensor bis-5HT-DTPA (Gd) with localized polymerization at sites of inflammation [43]; fluorescent protease was also used to sense cathepsin protease activity for showing the progression of necrotic core and neovascularization through fluorescence molecular tomography (FMT)-CT [44]. All the above mentioned studies well manifest the reliability and potential of the active targeting approaches. However, dual-modality imaging probes with active targeting ability for combining MRI and optical imaging are still in great need for plaque imaging studies. In the current study, $Fe_3O_4$ nanoparticles have provided an ideal carrier for constructing the MRI/optical probe not only because of its intrinsic superparamagnetic property but also a large surface/volume ratio and numerous surface capping ligands for covalently binding with targeting molecules. By attaching Cy5.5 onto the surface of $Fe_3O_4$ nanoparticles, dual functional probes with both magnetic and optical properties were successfully obtained (Fig. 2d).

A large body of evidence explains the key role of macrophages in the formation, progression and pathogenicity of plaques [45]. Macrophages, differentiated from monocytes which migrate from peripheral circulation, can engulf low-density lipoprotein and turn

into foamy macrophages, which is important for driving the progress of atherosclerotic plaques [46]. Actually, high macrophage content in plaques is a characteristic of vulnerability to rupture [47,48]. Another factor contributing to thin cap is the smooth muscle cells which produce collagen to form stable fibrous cap, can be sensitized to apoptosis by proinflammatory cytokines secreted by activated macrophages [49]. In addition, macrophages' apoptosis might help generate the necrotic lipid core and propagate thrombosis by producing tissue factor-rich apoptotic bodies [50]. As macrophage burden has been reported to play a key role in vulnerable plaques [51,52], discovery of novel biomarkers suitable for macrophages imaging is undoubtedly valuable for providing new insights for the preventive of acute cardiovascular diseases. OPN is one of the most abundant proteins expressed by foamy macrophages closely related with vulnerable plaques, but not circulating monocytes [53]. As shown in Fig. 4a, immunofluorescence staining experiments demonstrated that OPN expression is higher at the Ox-LDL-stimulated RAW264.7 macrophages, which is widely taken as a foamy macrophage model. Semi-quantitative results based on western blot confirmed that the expression level of OPN in foamy macrophages is ~9 folds higher than that in normal macrophages (Fig. 4b). The upregulated OPN expression was also clearly observed from atherosclerotic plaque tissue of mouse model (Fig. S2). It is known that the overexpression of OPN increases the accumulation of macrophages [54] and enlarges the aortic lesion size [55]; while OPN expression was down-regulated, atherosclerotic lesions in the aorta became remarkably smaller than those in control group [56] and in the meantime, the accumulation of macrophages was notably decreased [57]. All the studies strongly suggest OPN level can be potentially useful for staging the atherosclerotic progress. As indicated by the signal of Cy5.5 in Fig. 4c and d, COD-MNPs show a much higher accumulation in the cytoplasm of Ox-LDL-stimulated macrophages in comparison to the control groups after 24 h incubation. Only slight uptake of COD-MNPs incubated normal macrophages and CID-MNPs incubated Ox-LDL-stimulated macrophages was observed, indicating an effective and specific recognition of COD-MNPs conjugates with foamy macrophages.

The *in vivo* fluorescence and MR imaging was performed after intravenous injection of COD-MNPs into $ApoE^{-/-}$ mice through tail vein. In comparison to the control group, HFD fed group receiving COD-MNPs exhibited stronger fluorescence signal intensity especially though slightly decreased upon prolonged observation. The following MRI studies confirmed the enhancement effect of COD-MNPs conjugates for plaque imaging through a $T_2$-weighted sequence. Moreover, Prussian blue staining of revealed that the COD-MNPs probes mainly located in the plaques, while the immunofluorescence staining of OPN further suggested that the active targeting of COD-MNPs conjugates was realized owing to the elevated expression of OPN.

Our previous work [18] has explored the efficacy of probes targeting vascular smooth muscle cells using Profilin-1 conjugated nanoparticles. In comparison with it, the innovation of this work is mainly present in the design, synthesis method and application of OPN-targeted probe. And for the *in vivo* fluorescence data, in the former work, HFD group's fluorescence intensity was almost $4.5 \times 10^9$ p/sec/cm$^2$/sr, while in our experiment, HFD group's fluorescence intensity was almost $7.5 \times 10^{10}$ p/sec/cm$^2$/sr, almost 10-fold of the former work. This promising results was the combination of well-established animal models, OPN's high expression in the plaque, and adequate conjugation of Cy5.5, *etc*. Based on these, we have made further progress in reflecting the real biological behavior of macrophage in vulnerable plaque *via* noninvasive molecular imaging.

## 5. Conclusion

In summary, we have successfully constructed a MRI/optical dual-modality probe for OPN-targeting based on iron oxide nanoparticles. *In vitro* cell experiments demonstrated that the resulting probes can specifically recognize foamy cells. *In vivo* animal model studies revealed that visualization of vulnerable plaques can be realized through intravenous injection of the nanoprobes. The low toxicity feature endows the $Fe_3O_4$ nanoparticle-based probe with a promising potential in noninvasive evaluation of early clinical cardiovascular events.

## Conflicts of interest

None.

## Acknowledgements

This work was supported by the National Key Research Program of China (2016YFA0100903), National Funds for Distinguished Young Scientists of China (81325009) and National Nature Science Foundation of China (No. 81500360, 81671731, 81530058, 81570272), Beijing Nature Science Foundation (No. 7152131), China Postdoctoral Science Foundation (2016T90990) .

## Appendix A. Supplementary data

Supplementary data related to this article can be found at http://dx.doi.org/10.1016/j.biomaterials.2016.10.011.

## References

[1] Global Status Report on Noncommunicable Diseases 2010, World Health Organization, Geneva, 2010.
[2] Avoiding Heart Attacks and Strokes: Don't Be a Victim - Protect Yourself, World Health Organization, 2006.
[3] P. Libby, Mechanisms of acute coronary syndromes and their implications for therapy, N. Engl. J. Med. 368 (2013) 2004–2013.
[4] A.V. Finn, M. Nakano, J. Narula, F.D. Kolodgie, R. Virmani, Concept of vulnerable/unstable plaque, Arterioscler. Thromb. Vasc. Biol. 30 (2010) 1282–1292.
[5] Z.J. Zheng, J.B. Croft, W.H. Giles, G.A. Mensah, Sudden cardiac death in the United States, 1989–1998, Circulation 104 (2001) 2158–2163.
[6] M.A. Hlatky, P.S. Douglas, N.L. Cook, B. Wells, E.J. Benjamin, K. Dickersin, D.C. Goff, A.T. Hirsch, E.M. Hylek, E.D. Peterson, V.L. Roger, J.V. Selby, J.E. Udelson, M.S. Lauer, Future directions for cardiovascular disease comparative effectiveness research: report of a workshop sponsored by the National Heart, Lung, and Blood Institute, J. Am. Coll. Cardiol. 60 (2012) 569–580.
[7] J.L. Fleg, G.W. Stone, Z.A. Fayad, J.F. Granada, T.S. Hatsukami, F.D. Kolodgie, J. Ohayon, R. Pettigrew, M.S. Sabatine, G.J. Tearney, S. Waxman, M.J. Domanski, P.R. Srinivas, J. Narula, Detection of high-risk atherosclerotic plaque: report of the NHLBI Working Group on current status and future directions, JACC Cardiovasc. Imaging 5 (2012) 941–955.
[8] T. Quillard, P. Libby, Molecular imaging of atherosclerosis for improving diagnostic and therapeutic development, Circ. Res. 111 (2012) 231–244.
[9] F. Leuschner, M. Nahrendorf, Molecular imaging of coronary atherosclerosis and myocardial infarction: considerations for the bench and perspectives for the clinic, Circ. Res. 108 (2011) 593–606.
[10] S. Bjorkerud, B. Bjorkerud, Apoptosis is abundant in human atherosclerotic lesions, especially in inflammatory cells (macrophages and T cells), and may contribute to the accumulation of gruel and plaque instability, Am. J. Pathol. 149 (1996) 367–380.
[11] E. Thorp, M. Subramanian, I. Tabas, The role of macrophages and dendritic cells in the clearance of apoptotic cells in advanced atherosclerosis,, Eur. J. Immunol. 41 (2011) 2515–2518.
[12] F.D. Kolodgie, R. Virmani, A.P. Burke, A. Farb, D.K. Weber, R. Kutys, A.V. Finn, H.K. Gold, Pathologic assessment of the vulnerable human coronary plaque, Heart British Card. Soc. 90 (2004) 1385–1391.
[13] A. Franzen, D. Heinegard, Isolation and characterization of two sialoproteins present only in bone calcified matrix, Biochem. J. 232 (1985) 715–724.
[14] C.M. Giachelli, D. Lombardi, R.J. Johnson, C.E. Murry, M. Almeida, Evidence for a role of osteopontin in macrophage infiltration in response to pathological stimuli in vivo, Am. J. Pathol. 152 (1998) 353–358.
[15] M. Bidder, J.S. Shao, N. Charlton-Kachigian, A.P. Loewy, C.F. Semenkovich, D.A. Towler, Osteopontin transcription in aortic vascular smooth muscle cells

is controlled by glucose-regulated upstream stimulatory factor and activator protein-1 activities, J. Biol. Chem. 277 (2002) 44485–44496.
[16] E.R. O'Brien, M.R. Garvin, D.K. Stewart, T. Hinohara, J.B. Simpson, S.M. Schwartz, C.M. Giachelli, Osteopontin is synthesized by macrophage, smooth muscle, and endothelial cells in primary and restenotic human coronary atherosclerotic plaques, Arterioscler. Thromb. A J. Vasc. Biol. Am. Heart Assoc. 14 (1994) 1648–1656.
[17] A.R. Parrish, Ramos KS, Osteopontin mRNA expression in a chemically-induced model of atherogenesis, Ann. N. Y. Acad. Sci. 760 (1995) 354–356.
[18] Y. Wang, J. Chen, B. Yang, H. Qiao, L. Gao, T. Su, S. Ma, X. Zhang, X. Li, G. Liu, J. Cao, X. Chen, Y. Chen, F. Cao, In vivo MR and fluorescence dual-modality imaging of atherosclerosis characteristics in mice using Profilin-1 targeted magnetic nanoparticles, Theranostics 6 (2016) 272–286.
[19] X. Cai, X. Cai, C. Wang, B. Chen, W. Hua, F. Shen, L. Yu, Z. He, Y. Shi, Y. Chen, G. Xia, W. Bao, Y. Zhang, X. Wang, Antitumor efficacy of DMSA modified Fe3O4 magnetic nanoparticles combined with arsenic trioxide and adriamycin in Raji cells, J. Biomed. Nanotechnol. 10 (2014) 251–261.
[20] M. Zhang, Q. Zhao, Y. Gao, X. Wu, J. Wang, Prediction for rupture risk of carotid artery plaques: a comparative study of 3D-GSM and CAS system, Eur. J. Radiol. 85 (2016) 1659–1665.
[21] M.E. Kooi, V.C. Cappendijk, K.B. Cleutjens, A.G. Kessels, P.J. Kitslaar, M. Borgers, P.M. Frederik, M.J. Daemen, J.M. van Engelshoven, Accumulation of ultrasmall superparamagnetic particles of iron oxide in human atherosclerotic plaques can be detected by in vivo magnetic resonance imaging, Circulation 107 (2003) 2453–2458.
[22] R.R. Qiao, C.H. Yang, M.Y. Gao, Superparamagnetic iron oxide nanoparticles: from preparations to in vivo MRI applications, J. Mater. Chem. 19 (2009) 6274–6293.
[23] T.S. Lee, K.Y. Lu, Y.B. Yu, H.T. Lee, F.C. Tsai, Beta common receptor mediates erythropoietin-conferred protection on OxLDL-induced lipid accumulation and inflammation in macrophages, Mediat. Inflamm. 2015 (2015) 439759.
[24] J.C. Yabin Wang, Bo Yang, Hongyu Qiao, Lei Gao, Tao Su, Sai Ma, Xiaotian Zhang, Xiujuan Li, Gang Liu, Jianbo Cao, Xiaoyuan Chen, Yundai Chen, Feng Cao, In vivo MR and fluorescence dual-modality imaging of atherosclerosis characteristics in mice using Profilin-1 targeted magnetic nanoparticles, Theranostics 6 (2016) 272–286.
[25] A. Hoogi, D. Adam, A. Hoffman, H. Kerner, S. Reisner, D. Gaitini, Carotid plaque vulnerability: quantification of neovascularization on contrast-enhanced ultrasound with histopathologic correlation, AJR Am. J. Roentgenol. 196 (2011) 431–436.
[26] D. Staub, A.F. Schinkel, B. Coll, S. Coli, A.F. van der Steen, J.D. Reed, C. Krueger, K.E. Thomenius, D. Adam, E.J. Sijbrands, F.J. ten Cate, S.B. Feinstein, Contrast-enhanced ultrasound imaging of the vasa vasorum: from early atherosclerosis to the identification of unstable plaques, JACC Cardiovasc. Imaging 3 (2010) 761–771.
[27] R. Huang, S.S. Abdelmoneim, C.A. Ball, L.F. Nhola, A.M. Farrell, S. Feinstein, S.L. Mulvagh, Detection of carotid atherosclerotic plaque neovascularization using contrast enhanced ultrasound: a systematic review and meta-analysis of diagnostic accuracy studies, J. Am. Soc. Echocardiogr. Off. Publ. Am. Soc. Echocardiogr. 29 (2016) 491–502.
[28] C. Wenning, C. Kloth, M.T. Kuhlmann, A.H. Jacobs, O. Schober, S. Hermann, M.A. Schafers, Serial F-18-FDG PET/CT distinguishes inflamed from stable plaque phenotypes in shear-stress induced murine atherosclerosis, Atherosclerosis 234 (2014) 276–282.
[29] A. Irkle, A.T. Vesey, D.Y. Lewis, J.N. Skepper, J.L. Bird, M.R. Dweck, F.R. Joshi, F.A. Gallagher, E.A. Warburton, M.R. Bennett, K.M. Brindle, D.E. Newby, J.H. Rudd, A.P. Davenport, Identifying active vascular microcalcification by (18)F-sodium fluoride positron emission tomography, Nat. Commun. 6 (2015) 7495.
[30] R. Corti, J.I. Osende, J.T. Fallon, V. Fuster, G. Mizsei, H. Jneid, S.D. Wright, W.F. Chaplin, J.J. Badimon, The selective peroxisomal proliferator-activated receptor-gamma agonist has an additive effect on plaque regression in combination with simvastatin in experimental atherosclerosis: in vivo study by high-resolution magnetic resonance imaging, J. Am. Coll. Cardiol. 43 (2004) 464–473.
[31] M.V. McConnell, M. Aikawa, S.E. Maier, P. Ganz, P. Libby, R.T. Lee, MRI of rabbit atherosclerosis in response to dietary cholesterol lowering, Arterioscler. Thromb. Vasc. Biol. 19 (1999) 1956–1959.
[32] N. Singh, A.R. Moody, I. Roifman, D.A. Bluemke, A.E. Zavodni, Advanced MRI for carotid plaque imaging, Int. J. Cardiovasc. Imaging 32 (2016) 83–89.
[33] S. Mitragotri, J. Lahann, Physical approaches to biomaterial design, Nat. Mater. 8 (2009) 15–23.
[34] P. Bourrinet, H.H. Bengele, B. Bonnemain, A. Dencausse, J.M. Idee, P.M. Jacobs, J.M. Lewis, Preclinical safety and pharmacokinetic profile of ferumoxtran-10, an ultrasmall superparamagnetic iron oxide magnetic resonance contrast agent, Investig. Radiol. 41 (2006) 313–324.
[35] A.J. Lemke, M.I. Senfft von Pilsach, A. Lubbe, C. Bergemann, H. Riess, R. Felix, MRI after magnetic drug targeting in patients with advanced solid malignant tumors, Eur. Radiol. 14 (2004) 1949–1955.
[36] K. Morishige, D.F. Kacher, P. Libby, L. Josephson, P. Ganz, R. Weissleder, M. Aikawa, High-resolution magnetic resonance imaging enhanced with superparamagnetic nanoparticles measures macrophage burden in atherosclerosis, Circulation 122 (2010) 1707–1715.
[37] C. von Zur Muhlen, D. von Elverfeldt, N. Bassler, I. Neudorfer, B. Steitz, A. Petri-Fink, H. Hofmann, C. Bode, K. Peter, Superparamagnetic iron oxide binding and uptake as imaged by magnetic resonance is mediated by the integrin receptor Mac-1 (CD11b/CD18): implications on imaging of atherosclerotic plaques, Atherosclerosis 193 (2007) 102–111.
[38] I. Raynal, P. Prigent, S. Peyramaure, A. Najid, C. Rebuzzi, C. Corot, Macrophage endocytosis of superparamagnetic iron oxide nanoparticles: mechanisms and comparison of ferumoxides and ferumoxtran-10, Investig. Radiol. 39 (2004) 56–63.
[39] M. Nahrendorf, E. Keliher, P. Panizzi, H. Zhang, S. Hembrador, J.L. Figueiredo, E. Aikawa, K. Kelly, P. Libby, R. Weissleder, 18F-4V for PET-CT imaging of VCAM-1 expression in atherosclerosis, JACC Cardiovasc. Imaging 2 (2009) 1213–1222.
[40] K.C. Briley-Saebo, P.X. Shaw, W.J. Mulder, S.H. Choi, E. Vucic, J.G. Aguinaldo, J.L. Witztum, V. Fuster, S. Tsimikas, Z.A. Fayad, Targeted molecular probes for imaging atherosclerotic lesions with magnetic resonance using antibodies that recognize oxidation-specific epitopes, Circulation 117 (2008) 3206–3215.
[41] P.M. Winter, A.M. Neubauer, S.D. Caruthers, T.D. Harris, J.D. Robertson, T.A. Williams, A.H. Schmieder, G. Hu, J.S. Allen, E.K. Lacy, H. Zhang, S.A. Wickline, G.M. Lanza, Endothelial alpha(v)beta3 integrin-targeted fumagillin nanoparticles inhibit angiogenesis in atherosclerosis, Arterioscler. Thromb. Vasc. Biol. 26 (2006) 2103–2109.
[42] V. Amirbekian, M.J. Lipinski, K.C. Briley-Saebo, S. Amirbekian, J.G. Aguinaldo, D.B. Weinreb, E. Vucic, J.C. Frias, F. Hyafil, V. Mani, E.A. Fisher, Z.A. Fayad, Detecting and assessing macrophages in vivo to evaluate atherosclerosis noninvasively using molecular MRI, Proc. Natl. Acad. Sci. U. S. A. 104 (2007) 961–966.
[43] J.A. Ronald, J.W. Chen, Y. Chen, A.M. Hamilton, E. Rodriguez, F. Reynolds, R.A. Hegele, K.A. Rogers, M. Querol, A. Bogdanov, R. Weissleder, B.K. Rutt, Enzyme-sensitive magnetic resonance imaging targeting myeloperoxidase identifies active inflammation in experimental rabbit atherosclerotic plaques, Circulation 120 (2009) 592–599.
[44] M. Nahrendorf, P. Waterman, G. Thurber, K. Groves, M. Rajopadhye, P. Panizzi, B. Marinelli, E. Aikawa, M.J. Pittet, F.K. Swirski, R. Weissleder, Hybrid in vivo FMT-CT imaging of protease activity in atherosclerosis with customized nanosensors, Arterioscler. Thromb. Vasc. Biol. 29 (2009) 1444–1451.
[45] R.P. Choudhury, J.M. Lee, D.R. Greaves, Mechanisms of disease: macrophage-derived foam cells emerging as therapeutic targets in atherosclerosis, Nat. Clin. Pract. Cardiovasc. Med. 2 (2005) 309–315.
[46] G.K. Hansson, Inflammation, atherosclerosis, and coronary artery disease, N. Engl. J. Med. 352 (2005) 1685–1695.
[47] F.D. Kolodgie, H.K. Gold, A.P. Burke, D.R. Fowler, H.S. Kruth, D.K. Weber, A. Farb, L.J. Guerrero, M. Hayase, R. Kutys, J. Narula, A.V. Finn, R. Virmani, Intraplaque hemorrhage and progression of coronary atheroma, N. Engl. J. Med. 349 (2003) 2316–2325.
[48] B.D. MacNeill, I.K. Jang, B.E. Bouma, N. Iftimia, M. Takano, H. Yabushita, M. Shishkov, C.R. Kauffman, S.L. Houser, H.T. Aretz, D. DeJoseph, E.F. Halpern, G.J. Tearney, Focal and multi-focal plaque macrophage distributions in patients with acute and stable presentations of coronary artery disease, J. Am. Coll. Cardiol. 44 (2004) 972–979.
[49] P. Libby, Molecular and cellular mechanisms of the thrombotic complications of atherosclerosis, J. Lipid Res. 50 (Suppl) (2009) S352–S357.
[50] P. Libby, M. DiCarli, R. Weissleder, The vascular biology of atherosclerosis and imaging targets, Journal of nuclear medicine : official publication, Soc. Nucl. Med. vol. 51 (Suppl. 1) (2010), 33S-7S.
[51] P. Libby, M. Aikawa, Stabilization of atherosclerotic plaques: new mechanisms and clinical targets, Nat. Med. 8 (2002) 1257–1262.
[52] R. Virmani, A.P. Burke, A. Farb, F.D. Kolodgie, Pathology of the vulnerable plaque, J. Am. Coll. Cardiol. 47 (2006) C13–C18.
[53] M. Scatena, L. Liaw, C.M. Giachelli, Osteopontin: a multifunctional molecule regulating chronic inflammation and vascular disease, Arterioscler. Thromb. Vasc. Biol. 27 (2007) 2302–2309.
[54] K. Isoda, Y. Kamezawa, M. Ayaori, M. Kusuhara, N. Tada, F. Ohsuzu, Osteopontin transgenic mice fed a high-cholesterol diet develop early fatty-streak lesions, Circulation 107 (2003) 679–681.
[55] S. Chiba, H. Okamoto, S. Kon, C. Kimura, M. Murakami, M. Inobe, Y. Matsui, T. Sugawara, T. Shimizu, T. Uede, A. Kitabatake, Development of atherosclerosis in osteopontin transgenic mice, Heart Vessels 16 (2002) 111–117.
[56] Y. Matsui, S.R. Rittling, H. Okamoto, M. Inobe, N. Jia, T. Shimizu, M. Akino, T. Sugawara, J. Morimoto, C. Kimura, S. Kon, D. Denhardt, A. Kitabatake, T. Uede, Osteopontin deficiency attenuates atherosclerosis in female apolipoprotein E-deficient mice, Arterioscler. Thromb. Vasc. Biol. 23 (2003) 1029–1034.
[57] D. Bruemmer, A.R. Collins, G. Noh, W. Wang, M. Territo, S. Arias-Magallona, M.C. Fishbein, F. Blaschke, U. Kintscher, K. Graf, R.E. Law, W.A. Hsueh, Angiotensin II-accelerated atherosclerosis and aneurysm formation is attenuated in osteopontin-deficient mice, J. Clin. Investig. 112 (2003) 1318–1331.